AIAA Aviation Forum and ASCEND co-located Conference Proceedings
29 July - 2 August 2024, Las Vegas, Nevada
AIAA AVIATION FORUM AND ASCEND 2024

10.2514/6.2024-4480

Instability of two-species interfaces via vibration

Benjamin A. Wilfong*
Georgia Institute of Technology, Atlanta, GA, 30332 USA

Ryan M. McMullen[†] and Timothy Koehler[‡]
Sandia National Laboratories, Albuquerque, NM, 87185-0840 USA

Spencer H. Bryngelson[§]
Georgia Institute of Technology, Atlanta, GA, 30332 USA

Vibrating liquid–gas interfaces can break up due to hydrodynamic instability, resulting in gas injection into the liquid below it. The bubble injection phenomena can alter fluid-structural properties of mechanical assemblies and modify fuel composition. The primary Bjerknes force describes the seemingly counter-intuitive phenomenon that follows: gas bubbles sinking against buoyancy forces. The interface breakup that initializes the injection phenomenon is poorly understood and, as we show, depends on multiple problem parameters, including vibration frequency. This work uses an augmented 6-equation diffuse interface model with body forces and surface tension to simulate the initial breakup process. We show that a liquid–gas interface can inject a lighter gas into a heavier liquid, and that this process depends on parameters like the vibration frequency, vibration magnitude, and initial perturbation wavelength.

I. Introduction

The phases of multiphase fluid systems are often initially well-separated by an interface and become intermingled when the interface breaks up due to some form of agitation. The details of the interface breakup process can significantly impact the system's long-term behavior. For example, it can determine the efficacy of multiphase reactors [1] and is a necessary step in the formation of emulsions [2]. In other situations, interface breakup may be undesirable. Liquid-filled mechanical assemblies often contain a small amount of gas, and the breakup of the liquid-gas interface can result in unintended gas transport, drastically changing the fluid-structural behavior of the assembly [3, 4]. Consequently, understanding how interfaces break up is essential to predicting the behavior of multiphase fluid systems. Despite this fact, the physics of multiphase interface breakup is poorly understood.

This work presents linear stability analysis of three gravity-driven instabilities to guide two-dimensional simulations of liquid-gas interfaces subject to oscillatory accelerations. The results of this linear stability analysis suggest that the dominant mode of interface instability changes with different parameters of the initial perturbation and the applied oscillatory acceleration. The resulting growth rates inform which parameter sets should be simulated. Simulation results show that interface breakup for a given set of perturbation wavelengths and oscillation magnitude and frequency are only weakly dependent on the nature of periodic perturbation of the initial interface. The invariance of growth rate over several realizations of initial perturbations defined by smooth random noise is also observed.

We use a 6-equation diffuse interface model augmented with a surface tension model to perform full-resolution simulations of the early stages of liquid–gas interface breakup. A shock-capturing finite-volume scheme solves the diffuse interface model. The model is solved using HLL-type approximate Riemann solvers [5], high-order accurate WENO reconstructions [6], and high-order total variation diminishing (TVD) Runge–Kutta time steppers.

II. Theoretical Representation

Linear stability analysis of gravity-driven hydrodynamic instabilities provides insight into the rate at which early-stage growth should occur. The following sections detail the stability analysis of three instabilities: (1) Faraday instability, (2)

---

*Graduate Research Assistant, School of Computational Science and Engineering
[†]Senior Member of the Technical Staff, Engineering Sciences Center
[‡]Principal Member of the Technical Staff, Engineering Sciences Center
[§]Assistant Professor, School of Computational Science and Engineering, Daniel Guggenheim School of Aerospace Engineering

Rayleigh–Taylor instability with constant acceleration, and (3) Rayleigh–Taylor instability with oscillatory acceleration. Analyzing these instabilities identifies unstable regions in wavelength perturbation–oscillation period phase-space.

A. Linear Stability Analysis of the Faraday Instability

Consider an interface between a heavy and light fluid subject to the oscillatory acceleration

$$a = a_b + a_d \sin(\omega t)$$

where a_b is the constant background acceleration, taken to be $a_b = g = 9.81 \text{ m/s}^2$, a_d is the magnitude of the oscillatory component, and ω is the frequency of the oscillatory component. Floquet theory suggests [7] that, for a fluid of infinite depth, the oscillatory acceleration a_d required to excite a perturbation with wavenumber k at a growth rate s in a heavy fluid with density ρ, surface tension coefficient σ, and kinematic viscosity ν is given by

$$a_d(k, \omega, s) = \pm \left(\frac{|A_1|^2 + (A_0 A_1 + \overline{A_0 A_1})}{2|A_0|^2|A_1|^2} \pm \sqrt{\left(\frac{|A_1|^2 + (A_0 A_1 + \overline{A_0 A_1})}{2|A_0|^2|A_1|^2} \right)^2 - \frac{1}{|A_0|^2|A_1|^2}} \right)^{-1/2}$$

where

$$A_n = \frac{2}{k} \left[a_b k + \frac{\sigma}{\rho} k^3 + \nu^2 \left(q_n^4 + 2q_n^2 k^2 - 4q_n k^3 + k^4 \right) \right]$$

and

$$q_n^2 = k^2 + \frac{1}{\nu} \left[s + \mathrm{i}(\alpha + n)\omega \right],$$

where the positive root is taken by convention and α is taken to be $1/2$ to extract the sub-harmonic response. A perturbation wavelength-oscillation period phase space showing the growth rate given a target driving frequency magnitude a_t can be computed by solving the minimization problem

$$s = \arg\min_s |a_d(k, \omega, s) - a_t|.$$

using the simplex search method of Lagarias et al. [8].

B. Linear Stability Analysis of the Rayleigh–Taylor Instability with Constant Acceleration

The following analysis requires the introduction of the nondimensional Atwood number, defined as

$$\text{At} = \frac{\rho_h + \rho_l}{\rho_h - \rho_l},$$

where ρ_h and ρ_l are the densities of the heavier and lighter fluid respectively. A force balance at the perturbed interface between two fluids subject to a constant acceleration yields the following equation for the interface displacement ζ, [9]

$$\ddot{\zeta} = \text{At} k a_b \zeta - \frac{(\mu_h + \mu_l)}{\rho_h}(1 + \text{At})k^2 \dot{\zeta} - \sigma k^3 \frac{(1 + \text{At})}{2\rho_h}\zeta, \quad \text{with} \quad \zeta(0) = \epsilon, \ \dot{\zeta}(0) = 0, \tag{1}$$

where additional fluid properties μ_h and μ_l correspond to the dynamic viscosity of the heavier and lighter fluid, respectively, and ϵ is the small initial displacement of the interface. The corresponding asymptotic growth rate is given by the larger of the two roots of

$$\gamma_c^2 + \frac{\mu_1 + \mu_2}{\rho_2}(1 + \text{At})k^2 \gamma_c - \left[\text{At} k g - \sigma k^2 \frac{(1 + \text{At})}{2\rho_2} \right] = 0.$$

This relationship for the growth rates results from writing eq. (1) as a system of linear first-order differential equations and solving for the eigenvalues.

2
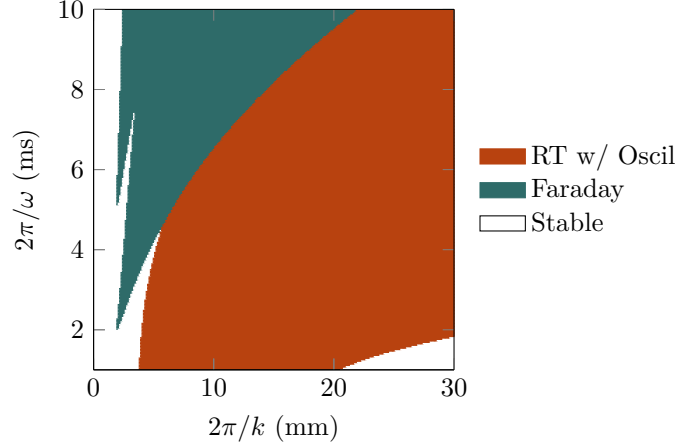
Fig. 1 The dominant growth mechanism in perturbation wavelength–oscillation period phase-space for oscillating acceleration with $a_d = 64g$

C. Linear Stability Analysis of the Rayleigh–Taylor Instability with Oscillatory Acceleration

Augmenting the force balance of section II.B with an additional oscillatory acceleration yields the following equation for the interface displacement

$$\ddot{\zeta} = \mathrm{At}\, k(a_b + a_d \sin(\omega t))\zeta - \frac{(\mu_1 + \mu_2)}{\rho_2}(1 + \mathrm{At})k^2 \dot{\zeta} - \sigma k^3 \frac{(1 + \mathrm{At})}{2\rho_2}\zeta, \quad \text{with} \quad \zeta(0) = \epsilon, \ \dot{\zeta}(0) = 0.$$

The resulting system of first-order differential equations with periodic coefficients is

$$\frac{\partial}{\partial t}\zeta = \frac{\partial}{\partial t}\begin{pmatrix} \zeta \\ \dot{\zeta} \end{pmatrix} = \begin{bmatrix} 0 & 1 \\ \mathrm{At}\, k(a_b + a_d \sin(\omega t)) - \sigma k^3 \dfrac{(1 + \mathrm{At})}{2\rho_h} & -\dfrac{(\mu_h + \mu_l)}{\rho_h}(1 + \mathrm{At})k^2 \end{bmatrix}\begin{pmatrix} \zeta \\ \dot{\zeta} \end{pmatrix}.$$

The monodromy matrix **M** can be found by advancing this system of ordinary differential equations in time for one period of oscillation (with period t_p) with initial conditions $\zeta_{t=0}^{(1)} = [1\ 0]^\top$ and $\zeta_{t=0}^{(2)} = [0\ 1]^\top$ and storing the results at $t = t_p$ as the columns of $\mathbf{M} = \left[\zeta_{t=t_p}^{(1)} \ \zeta_{t=t_p}^{(2)}\right]$. Floquet theory [10] suggests that for a system of ordinary differential equations with periodic coefficients, the solution at time $t + t_p$ can be determined from the solution at time t via the relationship

$$\zeta(t + t_p) = \zeta(t)\mathbf{M}.$$

The monodromy matrix eigenvalues $\exp(\mu_i)$ are the Floquet multipliers. If t is zero, the Floquet multipliers associated with time-advancing ODE for one period of oscillation with initial conditions $\zeta_{t=0}^{(1)}$ and $\zeta_{t=0}^{(2)}$ specify the geometric growth of the initial condition over a time period of t_p. The growth rate of the Rayleigh-Taylor instability with oscillatory acceleration, γ_d, is thus given by $\gamma_d = \max_i \mathrm{Re}\left(\ln(\exp(\mu_i))/t_p\right)$.

D. Stability Regimes

Exponential growth rates are used to visualize the phase space formed by the wavelength of the initial perturbation and the period of the oscillatory acceleration. They also indicate how different combinations of initial perturbation wavelength and period of oscillation at a given oscillating acceleration magnitude might affect the dominant instability, leading to interface breakup.

Figure 1 shows the dominant mode of instability in this phase space for an oscillatory acceleration with magnitude $a_d = 64g$. Note that while we include the stability analysis for the Rayleigh–Taylor instability without an oscillatory acceleration for completeness, no combination of perturbation wavelength and oscillation period in this limited phase-space results in Rayleigh–Taylor with constant acceleration being the dominant mechanism of instability. The growth rates for the Rayleigh–Taylor instability with and without oscillation converge in the limit of long oscillation periods. At the oscillation frequencies in fig. 1, the high-amplitude oscillatory acceleration makes the background

3

acceleration driving the Rayleigh–Taylor instability with constant acceleration relatively insignificant, which explains why it doesn't appear as a dominant mode of instability in the presented phase space.

III. Physical Model

We utilize reduced Baer–Nunziato [11] type models to model multiphase flows via a diffuse interface capturing method. These methods allow for artificial diffusion between fluids at material interfaces but alleviates the need for careful mesh management, multiple flow solvers, and unique treatments to ensure conservation required by interface tracking schemes [12].

A. The 6-equation Model

The complete disequilibrium Baer–Nunziato model can be reduced to the 6-equation model of Saurel [13] by assuming velocity equilibrium between species. For two fluids, this model is

$$\frac{\partial \alpha_i \rho_i}{\partial t} + \nabla \cdot (\alpha_i \rho_i \boldsymbol{u}) = 0,$$

$$\frac{\partial \rho \boldsymbol{u}}{\partial t} + \nabla \cdot (\rho \boldsymbol{u}\boldsymbol{u} + p\boldsymbol{I}) = 0.$$

$$\frac{\partial \alpha_1 \rho_1 e_1}{\partial t} + \nabla \cdot (\alpha_1 \rho_1 e_1 \boldsymbol{u}) + \alpha_1 p_1 \cdot \nabla \boldsymbol{u} = -\mu p_I (p_2 - p_1),$$

$$\frac{\partial \alpha_2 \rho_2 e_2}{\partial t} + \nabla \cdot (\alpha_1 \rho_2 e_2 \boldsymbol{u}) + \alpha_2 p_2 \cdot \nabla \boldsymbol{u} = -\mu p_I (p_1 - p_2),$$

$$\frac{\partial \alpha_1}{\partial t} + \boldsymbol{u} \cdot \nabla \alpha_1 = \mu (p_1 - p_2)$$

where ρ and $\boldsymbol{u}$ are the mixture density and velocity and p_i, α_i, ρ_i, and e_i are the pressure, volume fraction, density, and internal energy of species i. The model is closed using the stiffened gas equation of state, which defines the pressure p_i in phase i as

$$p_i = (\gamma_i - 1)\rho_i e_i - \gamma_i \pi_{\infty,i}$$

where γ_i and $\pi_{\infty,i}$ are the ratio of specific heats and liquid stiffness in species i respectively. The stiffened gas equation of state is known to faithfully model many liquids and gases [14]. The interfacial pressure p_I is given by

$$p_I = \frac{z_2 p_1 + z_1 p_2}{z_1 + z_2},$$

where $z_i = \rho_i c_i$ is the acoustic impedance of phase i with speed of sound c_i, given by

$$c_i = \sqrt{\frac{\gamma_i (p_i + \pi_{\infty,i})}{\rho_i}}.$$

The mixture density ρ is closed by the usual mixing rule

$$\rho = \sum_i \alpha_i \rho_i.$$

B. Adding Body Forces and Surface Tension

Surface tension is introduced via the model of Schmidmayer et al. [15]. The capillary stress tensor $\boldsymbol{\Omega}$ is given by

$$\boldsymbol{\Omega} = -\sigma \left(\|\nabla c\|\boldsymbol{I} - \frac{\nabla c \otimes \nabla c}{\|\nabla c\|} \right)$$

4

where σ is the surface tension coefficient and c a color function, where $c = 0$ in the first species, and 1 in the second. The 6-equation model with body forces and surface tension for two fluids is then

$$\frac{\partial \alpha_i \rho_i}{\partial t} + \nabla \cdot (\alpha_i \rho_i \boldsymbol{u}) = 0,$$

$$\frac{\partial \rho \boldsymbol{u}}{\partial t} + \nabla \cdot (\rho \boldsymbol{u}\boldsymbol{u} + p\boldsymbol{I} + \boldsymbol{\Omega}) = -\rho \boldsymbol{g},$$

$$\frac{\partial \alpha_1 \rho_1 e_1}{\partial t} + \nabla \cdot (\alpha_1 \rho_1 e_1 \boldsymbol{u}) + \alpha_1 p_1 \cdot \nabla \boldsymbol{u} = -\mu p_I (p_2 - p_1),$$

$$\frac{\partial \alpha_2 \rho_2 e_2}{\partial t} + \nabla \cdot (\alpha_1 \rho_2 e_2 \boldsymbol{u}) + \alpha_2 p_2 \cdot \nabla \boldsymbol{u} = -\mu p_I (p_1 - p_2),$$

$$\frac{\partial (\rho E + \varepsilon_0)}{\partial t} + \nabla \cdot ((\rho E + \varepsilon_0 + P)\boldsymbol{u} + \boldsymbol{\Omega} \cdot \boldsymbol{u}) = -\rho(\boldsymbol{u} \cdot \boldsymbol{g}),$$

$$\frac{\partial \alpha_1}{\partial t} + \boldsymbol{u} \cdot \nabla \alpha_1 = \mu(p_1 - p_2),$$

$$\frac{\partial c}{\partial t} + \boldsymbol{u} \cdot \nabla c = 0,$$

for component i, where $\varepsilon_0 = \sigma \|\nabla c\|$ is the capillary energy, and $\boldsymbol{g}$ is the vector of applied accelerations with

$$g_i = g_{0,i} + s_i \sin(\omega_i t + \phi_i),$$

where $g_{0,i}$ is the background gravity, s_i is the acceleration magnitude, ω_i is the frequency of oscillation, and ϕ_i is a phase shift for the acceleration in the i-th direction. The mixture total energy E is given by

$$E = e + \frac{\|\boldsymbol{u}\|^2}{2} \quad \text{where} \quad e = \sum_i Y_i e_i,$$

where $Y_i = \alpha_i \rho_i / \rho$ are the mass fractions of each phase. Surface tension and body forces are applied only to the mixture energy equation and not the internal energy equations because they are mixture characteristics, i.e., surface tension and body forces do not contribute to the internal energy of each species, but only the total mixture energy.

IV. Numerical Method

A. Finite volume method

A finite volume scheme that follows Coralic and Colonius [16] solves the model of section III.B. It is implemented in MFC [17], a GPU-based compressible CFD solver [18–20]. The computational domain is partitioned on a rectilinear grid where each cell has dimensions

$$D_{m,n,p} = \left[x_{m-1/2}, x_{m+1/2} \right] \times \left[y_{n-1/2}, y_{n+1/2} \right] \times \left[z_{p-1/2}, z_{p+1/2} \right]$$

and grid spacing

$$\Delta x_m = x_{m+1/2} - x_{m-1/2}, \quad \Delta y_n = y_{n+1/2} - y_{n-1/2}, \quad \Delta z_p = z_{p+1/2} - z_{p-1/2}.$$

The governing equations are discretized on the rectilinear grid as

$$\frac{\partial \boldsymbol{q}}{\partial t} + \frac{\partial \boldsymbol{F}^x(\boldsymbol{q})}{\partial x} + \frac{\partial \boldsymbol{F}^y(\boldsymbol{q})}{\partial y} + \frac{\partial \boldsymbol{F}^z(\boldsymbol{q})}{\partial z} = s(\boldsymbol{q}) - \boldsymbol{h}(\boldsymbol{q})\nabla \cdot \boldsymbol{u}, \quad (2)$$

where $\boldsymbol{q}$ and $\boldsymbol{F}$ are the vectors of conservative variables and fluxes. Equation (2) is integrated in space across each cell center as

$$\frac{\partial \boldsymbol{q}_{m,n,p}}{\partial t} = \frac{1}{\Delta x_j} \left(\boldsymbol{F}^x_{m-1/2,n,p} - \boldsymbol{F}^x_{m+1/2,n,p} \right) + \frac{1}{\Delta y_j} \left(\boldsymbol{F}^y_{m,n-1/2,p} - \boldsymbol{F}^y_{m,n+1/2,p} \right)$$

$$+ \frac{1}{\Delta z_k} \left(\boldsymbol{F}^z_{m,n,p-1/2} - \boldsymbol{F}^z_{m,n,p+1/2} \right) + s(q_{m,n,p}) - \boldsymbol{h}(\boldsymbol{q}_{m,n,p}) \left(\nabla \cdot \boldsymbol{u} \right)_{m,n,p}$$

5

where the $q_{m,n,p}$, $s(q_{m,n,p})$, and $h(q_{m,n,p})$ are the volume average conservative variables and source terms, which for the 6-equation model with surface tension and body forces are given by

$$
q_{m,n,p} = \begin{pmatrix} \alpha_1\rho_1 \\ \alpha_2\rho_2 \\ \rho u \\ \alpha_1\rho_1 e_1 \\ \alpha_2\rho_2 e_2 \\ \rho E + \varepsilon_0 \\ \alpha_1 \\ c \end{pmatrix}_{m,n,p}
\qquad
s(q_{m,n,p}) = \begin{pmatrix} 0 \\ 0 \\ -\rho g \\ -\mu p_I(p_2 - p_1) \\ -\mu P_I(p_1 - p_2) \\ -\rho(u \cdot g) \\ \mu(p_1 - p_2) \\ 0 \end{pmatrix}_{m,n,p}
\qquad
h(q_{m,n,p}) = \begin{pmatrix} 0 \\ 0 \\ \mathbf{0} \\ \alpha_1 p_1 \\ \alpha_2 p_2 \\ 0 \\ -\alpha_1 \\ -c \end{pmatrix}_{m,n,p}
$$

The flux terms F are obtained by averaging over cell interfaces.

B. Shock capturing reconstructions

Our numerical scheme requires reconstructing the conservative variables q and velocities u at the cell interfaces. The left and right states at each interface are then used to calculate the flux and velocity at the interface via

$$
F^x_{m+1/2,n,p} = F^x\left(q^L_{m+1/2,n,p}, q^R_{m+1/2,n,p}\right),
$$

$$
u^x_{m+1/2,n,p} = u^x\left(q^L_{m+1/2,n,p}, q^R_{m+1/2,n,p}\right).
$$

WENO reconstructions compute $q^L_{m+1/2,n,p}$ and $q^R_{m+1/2,n,p}$ in order to maintain accuracy and minimize interface smearing [6]. A $(2k-1)$th-order WENO reconstructed state variable $f_{m+1/2,n,p}$ is derived from a weighted sum of k candidate polynomials as

$$
f_{m+1/2,n,p} = \sum_{r=0}^{k} \omega^R_{m+1/2} f^R_{m+1/2,n,p}.
$$

The ideal weights ω_R are obtained using smoothing indicators β^R. WENO reconstructions are susceptible to spurious oscillations at material interfaces because they are not total variation diminishing (TVD). We suppress these oscillations by reconstructing primitive variables $(\rho_1, \rho_2, u, e_1, e_2, E, \alpha_1, c)^\top$ rather than the conservative variables q. An identical procedure is performed in the y-direction with subscripts $(n, m + 1/2, p)$ and in the z-direction with subscripts $(m, n, p + 1/2)$.

C. Approximate Riemann solver

The Riemann problem is solved using a Harten–Lax–van Leer contact (HLLC) approximate Riemann solver [21]. The HLLC Riemann solver allows for three discontinuities with wave speeds s_L, s_R, and s_* in the left, right, and star states of the Riemann solver, which are estimated using the quantities $q^L_{m+1/2,n,p}$ and $q^R_{m+1/2,n,p}$. The state at the cell interface is given by

$$
q_{m+1/2,n,p} = \begin{cases} q^L_{m+1/2,n,p} & 0 \le s_L \\ q^{L^*}_{m+1/2,n,p} & s_L \le 0 \le s_* \\ q^{R^*}_{m+1/2,n,p} & s_* \le 0 \le s_R \\ q^R_{m+1/2,n,p} & 0 \ge s_R \end{cases}.
$$

The intermediate states $q^{L^*}_{m+1/2,n,p}$ and $q^{R^*}_{m+1/2,n,p}$ are calculated by assuming that the normal velocity and pressure are continuous across the contact discontinuity. The flux at the cell interface is then

$$
F(q_{m+1/2,n,p}) = \begin{cases} F(q^L_{m+1/2,n,p}) & 0 \le s_L \\ F(q^L_{m+1/2,n,p}) + s_L\left(q^{L^*}_{m+1/2,n,p} - q^L_{m+1/2,n,p}\right) & s_L \le 0 \le s_* \\ F(q^R_{m+1/2,n,p}) + s_R\left(q^{R^*}_{m+1/2,n,p} - q^R_{m+1/2,n,p}\right) & s_* \le 0 \le s_R \\ F(q^R_{m+1/2,n,p}) & 0 \ge s_R \end{cases}.
$$

An identical procedure is performed in the y-direction with subscripts $(n, m + 1/2, p)$ and in the z-direction with subscripts $(m, n, p + 1/2)$.

D. Time stepping

The conservative variables $\boldsymbol{q}$ are integrated in time using the third-order accurate total variation diminishing (TVD) and strong stability preserving (SSP) Runge–Kutta time stepper [22].

$$\boldsymbol{q}_{m,n,p}^{(1)} = \boldsymbol{q}_{m,n,p}^{h} + \Delta t \frac{\partial \boldsymbol{q}_{m,n,p}^{n}}{\partial t},$$

$$\boldsymbol{q}_{m,n,p}^{(2)} = \frac{3}{4}\boldsymbol{q}_{m,n,p}^{h} + \frac{1}{4}\boldsymbol{q}_{m,n,p}^{(1)} + \frac{1}{4}\Delta t \frac{\partial \boldsymbol{q}_{m,n,p}^{(1)}}{\partial t},$$

$$\boldsymbol{q}_{m,n,p}^{h+1} = \frac{1}{3}\boldsymbol{q}_{m,n,p}^{h} + \frac{2}{3}\boldsymbol{q}_{m,n,p}^{(2)} + \frac{2}{3}\Delta t \frac{\partial \boldsymbol{q}_{m,n,p}^{(2)}}{\partial t},$$

where $\boldsymbol{q}_{m,n,p}^{(l)}$ denote intermediate states. The TVD and SSP properties of this Runge–Kutta time stepper allow for capturing discontinuities and shocks without introducing oscillations in time.

V. Results

A. Validation

Implementation of these methods has been validated extensively against experimental results on test cases such as shock–bubble interaction, shock–droplet interaction, spherical bubble dynamics, and isentropic and Taylor–Green vortices [17]. The additional physics introduced in the 6-equation model with body forces and surface tension have been validated against exact solutions for the pressure equilibration of a water droplet in air and the growth rate of a Rayleigh-Taylor instability.
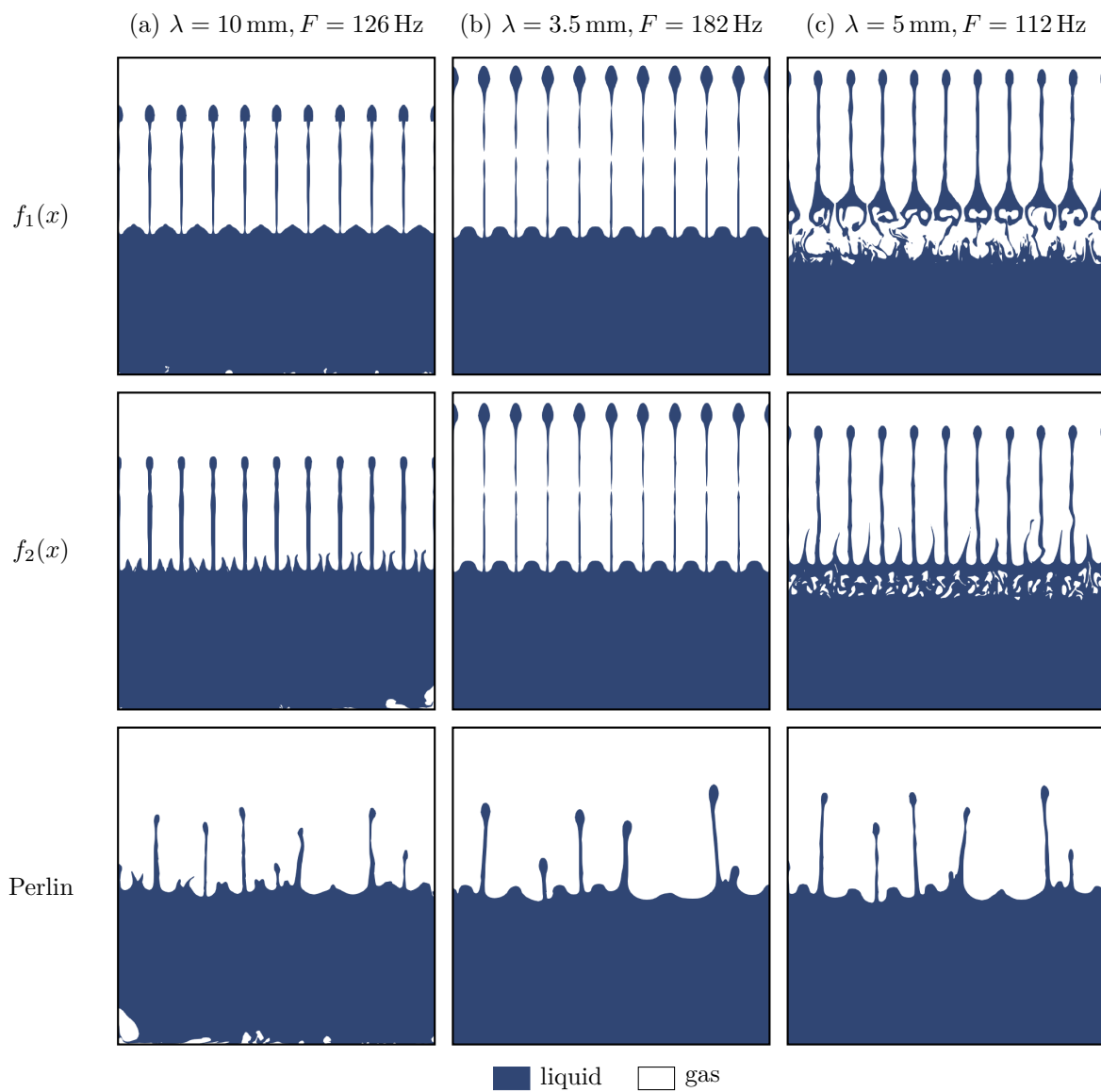
B. Interface Breakup

In what follows, we present quantitative results detailing the early breakup of a liquid–gas interface for three unique initial perturbations. The x and y coordinates are parallel and perpendicular to the interface. The initial condition is made of gas with fluid properties $(\rho, \gamma, \pi_\infty, \sigma) = (1\,\text{kg/m}^3, 1.4, 0\,\text{Pa}, 0.0206\,\text{N/m})$ and liquid with fluid properties $(\rho, \gamma, \pi_\infty, \sigma) = (1000\,\text{kg/m}^2, 6.12, 3.43 \times 10^8\,\text{Pa}, 0.0206\,\text{N/m})$ separated by an interface at $5\lambda + \epsilon f(x)$ in a $10\lambda \times 10\lambda$ domeina, where λ is the wavelength of the initial perturbation. $f(x)$ is a function that describes a perturbation, and ϵ is a parameter used to specify the thickness of the initial perturbation at $\lambda/20$. Pressure is initialized such that is satisfies a hydrodynamic equilibrium with a pressure of $100\,\text{kPa}$ at the interface.

There are two initial perturbations in this study that are explicit functions of the horizontal coordinate x. These perturbations are described by

$$f_1(x) = \frac{1}{2}\sin\left(\frac{2\pi x}{\lambda} - \frac{\pi}{2}\right) \quad \text{and} \quad f_2(x) = \pi \exp\left[\sin\left(\frac{2\pi x}{\lambda} - \frac{\pi}{2}\right) - 2\right] - 0.656$$

where constants center each explicit perturbation at $f_i(x) = 0$ and result in $f_i(x) \in [-0.5, 0.5]$. $f_1(x)$ was selected as the perturbation assumed by the linear stability analysis, and $f_2(x)$ was chosen to determine whether different smooth, periodic initial conditions yield different interfacial breakups. The third type of perturbation is Perlin noise [23], a procedurally generated smooth random noise often used for natural terrain generation and texturing in computer graphics. Perlin noise is random and procedurally generated, so no explicit equation exists. Its properties make it well suited to creating natural random interfaces and promoting asymmetric interface breakups.

Figure 2 shows the qualitative nature of interface breakup for three parings of initial perturbation wavelength and oscillation frequency subject to acceleration with an oscillatory component $a_d = 64g$ and a constant component $a_b = g$. Regions in blue represent the gas phase, while regions in white represent the liquid phase. Note that for these results, the same Perlin noise was scaled and used for all parameter pairings. The first noteworthy detail in Figure 2 is the supposed entrainment of gas at the bottom of the domain in all three $\lambda = 10\,\text{mm}$ simulations. This results from the simple extrapolation-based boundary conditions used in these simulations combined with the larger grid spacing used

Fig. 2 Breakup of interfaces with different initial perturbation wavelengths and perturbation methods subject to acceleration with an oscillatory component $a_d = 64g$ and a constant component $a_b = g$.

8
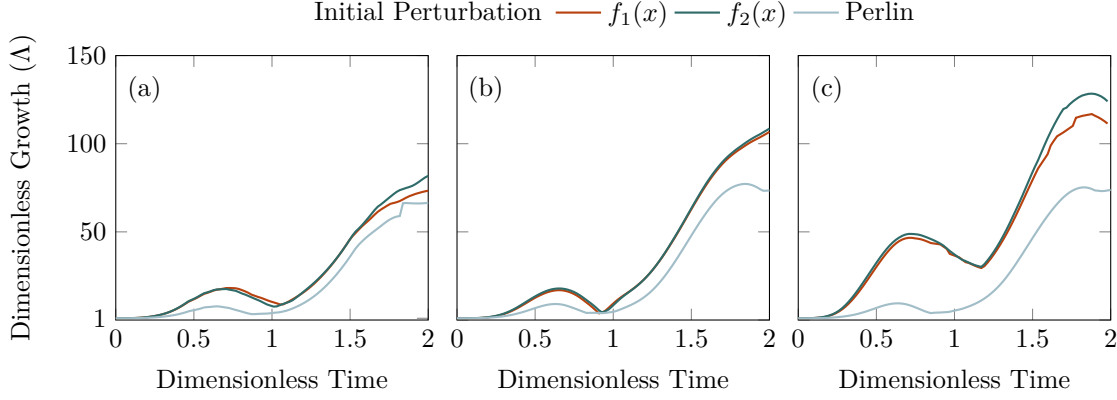
Fig. 3 Dimensionless growth of interfaces subjected to acceleration with an oscillatory component $a_d = 64g$ and constant component $a_b = g$ for parameter sets (a)–(c).

for this longer perturbation wavelength, which allow the liquid phase to be separated from the bottom boundary by non-physical pressure waves moving throughout the computational domain. More noteworthy is the entrainment of gas in the liquid phase shown in the $\lambda = 5$ mm case for the interfaces described by $f_1(x)$ and $f_2(x)$. The $f_1(x)$ case shows entrainment resulting from the detachment of the liquid layer at the interface, while the $f_2(x)$ case shows entrainment that appears more like bubbles rather than near complete detachment of the jets shown in the $f_1(x)$ results.

Figure 3 shows the growth of the interface thickness as a function of time non-dimensionalized in space by the initial perturbation thickness and in time by the period of oscillation for the configurations described above. For all cases, interface thickness is calculated as $\Delta = y_{\max} - y_{\min}$ where $y_{\max}$ and $y_{\min}$ are the maximum and minimum y-coordinates of a contour at $\alpha_1 = 0.5$. The dimensionless growth Λ is defined as $\Lambda \equiv \Delta(t)/\Delta(t = 0)$. The interface perturbed by Perlin noise grows slower for all three parameter sets than the two periodic perturbations. The reason for this is revealed by taking a Fast Fourier Transform of the initial perturbations. The Fast Fourier Transform of the smooth random interface indicates that it has dominant Fourier modes at lower frequencies than the explicit perturbations $f_1(x)$ and $f_2(x)$. These lower-frequency Fourier modes correspond to longer wavelengths in space. The stability analysis predicts that in the neighborhoods around the perturbation wavelengths used for these simulations, an increase in wavelength leads to a decrease in growth rate.

Another result of interest is the invariant response to mean statistics over time for different realizations of Perlin noise. For this, four previously unused realizations of Perlin Noise were generated and used to separate the contents of a square domain subject to acceleration having an oscillatory component with frequency and magnitude $\omega = 112$ Hz and $a_d = 128g$ and a constant component with $a_b = g$. The qualitative features of the interfacial breakup for the four unique realizations of Perlin Noise are shown in fig. 4, and the accompanying quantitative dimensionless growth is given in fig. 5. While the morphological details of the interface breakup depend on the realization of Perlin noise used to define the initial perturbation, statistical measures, e.g., the overall growth of the interface, are relatively insensitive to the realization of Perlin noise. This invariance is further supported by the similarity in the growth of the interfaces shown in fig. 5. All four realizations of Perlin Noise develop at similar rates and to a similar maximum dimensionless displacement.

VI. Conclusion

The downward motion of gasses in liquids due to the Bjerknes force can significantly impact the damping and resonance of vibrated hydrodynamic systems. This change in damping and resonance can cause hydrodynamic systems to experience forces many times greater than expected, which can cause unexpected regions of high pressure and deformation of physical containers. Understanding the initial breakup of the interface and the injection of bubbles is important for better understanding these systems. Linear stability analysis is fundamental to understanding the earliest stages of interface breakup. It aids in selecting test cases and identifying dominant modes of instability. However, this theory is linear, so full-resolution numerical simulations are required to observe gas entrainment and bubble motion. We show that our model and numerical method can simulate the injection of gasses into liquids. We also compare the liquid–gas early-stage interface breakup for three different initial perturbations and show that a smooth random

9
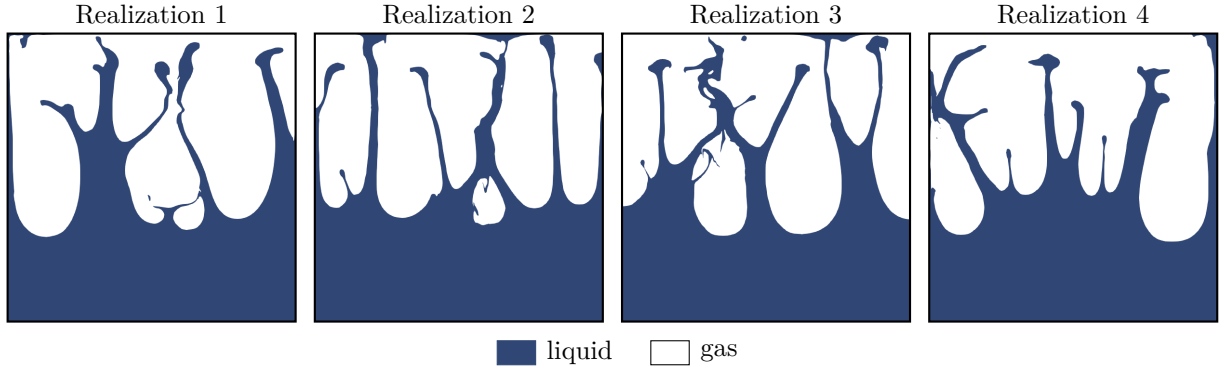
Fig. 4   Breakup of four unique Perlin noise interfaces subject to acceleration with an oscillatory component $a_d = 128g$ and a constant component $a_b = g$.
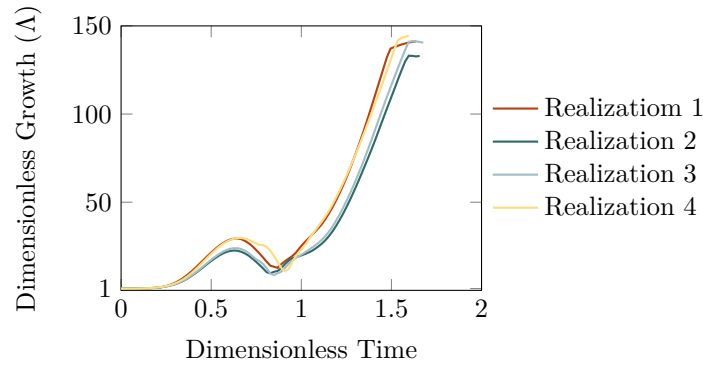
Fig. 5   Dimensionless growth for the four unique realizations of Perlin noise in fig. 4 subject to acceleration with an oscillatory component $a_d = 128g$ and a constant component $a_b = g$.

perturbation yields similar growth behavior for several unique realizations. To reach these results, we augment a 6-equation multiphase flow model to include the effects of surface tension and gravity. The presented results will help inform the next steps of this research, which include exploring other possible random perturbations and extending them to three dimensions.

Acknowlegements

accepting the article for publication, acknowledges that the United States Government retains a non-exclusive, paid-up, irrevocable, world-wide license to publish or reproduce the published form of this article or allow others to do so, for United States Government purposes. The DOE will provide public access to these results of federally sponsored research in accordance with the DOE Public Access Plan https://www.energy.gov/downloads/doe-public-access-plan.

References

[1] Krishna, R., and Sie, S., "Strategies for multiphase reactor selection," *Chemical Engineering Science*, Vol. 49, No. 24, Part A, 1994, pp. 4029–4065.

[2] Taylor, G. I., "The formation of emulsions in definable fields of flow," *Proceedings of the Royal Society of London. Series A, Containing Papers of a Mathematical and Physical Character*, Vol. 146, No. 858, 1934, pp. 501–523.

[3] Romero, L. A., Torczynski, J. R., Clausen, J. R., O'Hern, T. J., and Benavides, G. L., "Gas-Enabled Resonance and Rectified Motion of a Piston in a Vibrated Housing Filled With a Viscous Liquid," *Journal of Fluids Engineering*, Vol. 138, No. 6, 2016, p. 061302.

[4] Torczynski, J. R., O'Hern, T. J., Clausen, J. R., and Koehler, T. P., "Gas-Induced Motion of a Piston in a Vibrated Liquid-Filled Housing," *Journal of Fluids Engineering*, Vol. 141, No. 9, 2019, p. 091106.

[5] Toro, E., *Riemann Solvers and Numerical Methods for Fluid Dynamics: A Practical Introduction*, Springer Berlin Heidelberg, 2009.

[6] Shu, C.-W., "Numerical methods for hyperbolic conservation laws (AM257)," , 2006. Lecture notes.

[7] Kumar, K., "Linear theory of Faraday instability in viscous liquids," *Proceedings: Mathematical, Physical and Engineering Sciences*, Vol. 452, No. 1948, 1996, pp. 1113–1126.

[8] Lagarias, J. C., Reeds, J. A., Wright, M. H., and Wright, P. E., "Convergence Properties of the Nelder-Mead Simplex Method in Low Dimensions," *SIAM J. Optim.*, Vol. 9, 1998, pp. 112–147.

[9] Piriz, A. R., Cortázar, O. D., López Cela, J. J., and Tahir, N. A., "The Rayleigh–Taylor instability," *American Journal of Physics*, Vol. 74, No. 12, 2006, pp. 1095–1098.

[10] Brown, B. M., Eastham, M. S. P., and Schmidt, K. M., *Floquet Theory*, Springer Basel, Basel, 2013, pp. 1–29.

[11] Andrianov, N., and Warnecke, G., "The Riemann problem for the Baer–Nunziato two-phase flow model," *Journal of Computational Physics*, Vol. 195, No. 2, 2004, pp. 434–464.

[12] Saurel, R., and Pantano, C., "Diffuse-interface capturing methods for compressible two-phase flows," *Annual Review of Fluid Mechanics*, Vol. 50, No. 1, 2018, p. 105–130.

[13] Saurel, R., Petitpas, F., and Berry, R. A., "Simple and efficient relaxation methods for interfaces separating compressible fluids, cavitating flows and shocks in multiphase mixtures," *Journal of Computational Physics*, Vol. 228, No. 5, 2009, pp. 1678–1712.

[14] Le Métayer, O., and Saurel, R., "The Noble–Abel stiffened-gas equation of state," *Physics of Fluids*, Vol. 28, No. 4, 2016, p. 046102.

[15] Schmidmayer, K., Petitpas, F., Daniel, E., Favrie, N., and Gavrilyuk, S., "A model and numerical method for compressible flows with capillary effects," *Journal of Computational Physics*, Vol. 334, 2017, pp. 468–496.

[16] Coralic, V., and Colonius, T., "Finite-volume WENO scheme for viscous compressible multicomponent flows," *Journal of Computational Physics*, Vol. 274, 2014, pp. 95–121.

[17] Bryngelson, S. H., Schmidmayer, K., Coralic, V., Meng, J. C., Maeda, K., and Colonius, T., "MFC: An open-source high-order multi-component, multi-phase, and multi-scale compressible flow solver," *Comp. Phys. Comm.*, Vol. 266, 2021, p. 107396.

[18] Elwasif, W., Godoy, W., Hagerty, N., Harris, J. A., Hernandez, O., Joo, B., Kent, P., Lebrun-Grandie, D., Maccarthy, E., Melesse Vergara, V., et al., "Application experiences on a GPU-accelerated Arm-based HPC testbed," *Proceedings of the HPC Asia 2023 Workshops*, 2023, pp. 35–49.

[19] Radhakrishnan, A., Le Berre, H., and Bryngelson, S. H., "Scalable GPU accelerated simulation of multiphase compressible flow," *The International Conference for High Performance Computing, Networking, Storage, and Analysis (SC)*, Dallas, TX, USA, 2022, pp. 1–3.

[20] Radhakrishnan, A., Le Berre, H., Wilfong, B., Spratt, J.-S., Rodriguez Jr., M., Colonius, T., and Bryngelson, S. H., "Method for portable, scalable, and performant GPU-accelerated simulation of multiphase compressible flow," *Computer Physics Communications*, Vol. 302, 2024, p. 109238.

[21] Toro, E. F., "The HLLC Riemann solver," *Shock Waves*, Vol. 29, No. 8, 2019, pp. 1065–1082.

[22] Gottlieb, S., and Shu, C.-W., "Total variation diminishing Runge–Kutta schemes," *Mathematics of Computation*, Vol. 67, No. 221, 1998, pp. 73–85.

[23] Perlin, K., "Improving noise," *ACM Trans. Graph.*, Vol. 21, No. 3, 2002, p. 681–682.